

Article

Integrating a Physical Model with Multi-Objective Optimization for the Design of Optical Angle Nano-Positioning Mechanism

Bo Jiang ¹, Yiming Dong ^{1,2}, Zijie Zhang ^{1,3}, Xiangyu Li ¹, Yuxuan Wei ¹, Yifan Guo ^{1,3} and Haixia Liu ^{4,*}

¹ Xi'an Institute of Optics and Precision Mechanics, Chinese Academy of Sciences, Xi'an 710119, China; ilysay@opt.ac.cn (B.J.); ymdong23@163.com (Y.D.); zzzj98ab@163.com (Z.Z.); lixiangyu@opt.ac.cn (X.L.); weiyuxuan@opt.ac.cn (Y.W.); 15935138528@163.com (Y.G.)

² University of Chinese Academy of Sciences, Beijing 100049, China

³ School of Opto-Electrical Engineering, Xi'an Technological University, Xi'an 710021, China

⁴ School of Mechanical and Electrical Engineering, Xi'an University of Architecture and Technology, Xi'an 710055, China

* Correspondence: liuhx_12@163.com

Abstract: In light of recent advancements in synchrotron radiation technology and nano-technology, there has been a marked increase in the need for ultra-precision nano-positioning mechanisms. This paper presents a method that integrates physical models with multi-objective optimization for developing an optical angle nano-positioning mechanism. We begin by examining the actual motion law of the mechanism, based on kinematic principles. The outcomes from this kinematic analysis facilitate a static analysis of the flexible hinge, identified as a critical component of the mechanism. Subsequently, we establish a dynamic model for the entire mechanism. By employing the physical model as a base and combining it with the optimization algorithm, we identify the optimal design parameters for the mechanism. The design achieves a resolution of 50 nrad and meets the specified requirements. The first-order inherent frequency of the mechanism is approximately 43.75 Hz. There is a discrepancy of 2.63% from the finite element modal analysis results and a 3.33% difference from the theoretical analysis results, validating the reliability of the design method proposed in this study.

Keywords: nano-positioning mechanisms; synchrotron radiation facility; multi-objective optimization



Citation: Jiang, B.; Dong, Y.; Zhang, Z.; Li, X.; Wei, Y.; Guo, Y.; Liu, H. Integrating a Physical Model with Multi-Objective Optimization for the Design of Optical Angle Nano-Positioning Mechanism. *Appl. Sci.* **2024**, *14*, 3756. <https://doi.org/10.3390/app14093756>

Academic Editor: Francesco Enrichi

Received: 26 February 2024

Revised: 24 April 2024

Accepted: 26 April 2024

Published: 28 April 2024



Copyright: © 2024 by the authors. Licensee MDPI, Basel, Switzerland. This article is an open access article distributed under the terms and conditions of the Creative Commons Attribution (CC BY) license (<https://creativecommons.org/licenses/by/4.0/>).

1. Introduction

Compliant mechanisms (CMs) represent a significant area in modern mechanism design, characterized by high precision, high reliability, and absence of clearance, friction, or wear [1–4]. By enhancing the reduction ratio of CMs, it is possible to avoid friction and backlash errors typically associated with gear reducers, thereby effectively improving the resolution while maintaining accuracy [5]. Recently, mechanisms based on flexible designs have garnered considerable attention for applications in microscopic imaging [6,7] and micromanipulation [8–13].

The synchrotron radiation facility (SRF) marks a significant milestone in the development of human light sources, providing a new, high-performance, highly collimated, pure, and bright light source [14–16]. A monochromator, a core component of the synchrotron radiation device, separates the polychromatic light emitted by the source into the required monochromatic light [17], as depicted in Figure 1.

To achieve angular positioning of the monochromator splitter crystal, extensive research has been conducted. The Argonne National Laboratory's advanced photon source (APS) has developed a series of nano-positioning instruments [18–24]. Among these, CMs utilized in the artificially slotted crystal monochromator and the hard X-ray polarizer can attain angular resolutions of 20–40 nrad and 80 nrad, respectively, in angular adjustments. The European synchrotron radiation facility (ESRF) employs traditional slow-walking silk-cutting technology to fabricate the four-link straight circular flexhinge bending mechanism

in a single piece, achieving a focused light spot of less than 50 nm [25]. Utilizing CMs, the Shanghai synchrotron radiation facility (SSRF) has demonstrated the feasibility of creating micro displacement adjustment mechanisms for synchrotron radiation devices using 3D printing technology [26].

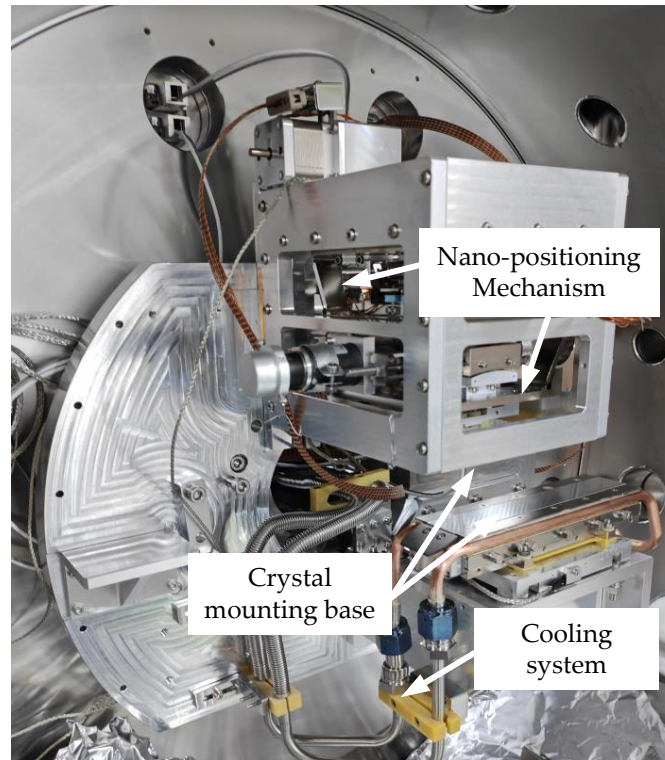


Figure 1. Internal structure of a monochromator. The main components are labeled.

The multi-objective optimization problem (MOOP) aims to address scenarios with multiple conflicting objectives by finding a solution that meets all optimization criteria. This is crucial for both theoretical research and practical engineering applications. Traditional methods for multi-objective optimization include the weighted sum method, constraint method, objective programming method, distance function method, and min-max method [27]. Traditional optimization techniques often struggle to guarantee excellent outcomes when solving MOOPs due to their inherent limitations. Consequently, the study of intelligent optimization algorithms, which are essentially stochastic search algorithms that mimic the behavior of natural biological groups, has garnered significant interest. These algorithms are particularly effective for tackling complex problems characterized by discontinuity, nonlinearity, and multiple variables.

In the application research of multi-objective optimization, Ehsan Naderi et al. developed a hybrid algorithm combining the random frog leaping algorithm (RFLA) and particle swarm optimization (PSO), achieving high solution quality [28]. Nguyen et al. utilized the nondominated sorting genetic algorithm-II (NSGA-II) to optimize the design of a compliant linear guide mechanism with a high-precision feed drive, achieving a closed-loop control error in output displacement of less than 0.02 μm [29]. Their team also applied NSGA-II to the design of micromachining feed drive mechanisms, producing and evaluating the optimization results [9]. Additionally, WANG et al. implemented the multi-objective particle swarm optimization (MOPSO) algorithm to design a planar parallel 3-DOF nano-positioner for scanning probe microscopy (SPM). The effectiveness of the proposed modeling and optimization methods was corroborated by both simulation and experimental results [30].

From the investigations discussed, it is evident that as the requirements for the monochromatic beam of synchrotron radiation devices continue to increase, so too do the technical demands on nano-scale micro-displacement tables. To meet the ultra-high

resolution micro-displacement needs of the SSRF, the compliant mechanism offers a solution capable of achieving ultra-precision motion, which is challenging to obtain with conventional motor servo systems. This paper employs a multi-objective optimization algorithm with the aim to minimize the driving force of the mechanism while maintaining a sufficiently high inherent frequency. The primary contribution of this study lies in the modeling and optimal design method for the nano-locator. The proposed method utilizes the NSGA-II to derive the Pareto front, and the optimal design parameters are subsequently selected based on this front. Following the determination of design parameters, a simulated and manufactured experimental prototype is used to validate the optimal design results.

The remainder of this paper is structured as follows: Section 2 establishes the mathematical model, capturing both the static and dynamic attributes of the mechanism. Section 3 presents the design metrics, evaluates the design parameters, and conducts a preliminary analysis. Section 4 outlines the objective equations and associated constraints. Section 5 details the solution computation using the MOOP algorithm and analyzes the simulation results. Section 6 displays the prototype validation compared to the design's optimization results. Finally, Section 7 offers a concise summary.

2. Optical Angle Nano-Positioning Mechanism Configuration

The machine developed in this study is designed to have a simple and reliable structure, extensive range of movement adjustment, and high inherent frequency. To fulfill these criteria, a trapezoidal four-link is implemented for high-precision adjustment and positioning within a restricted range. The design features include a fixed platform, four flexible link rods, a moving platform, and a driver. The fixed platform is securely mounted to the base platform. Upon application of a driving force F_{Σ} by the driver, the moving platform undergoes a micrometric displacement, resulting in an angular displacement around the pivot point, as depicted in Figure 2.

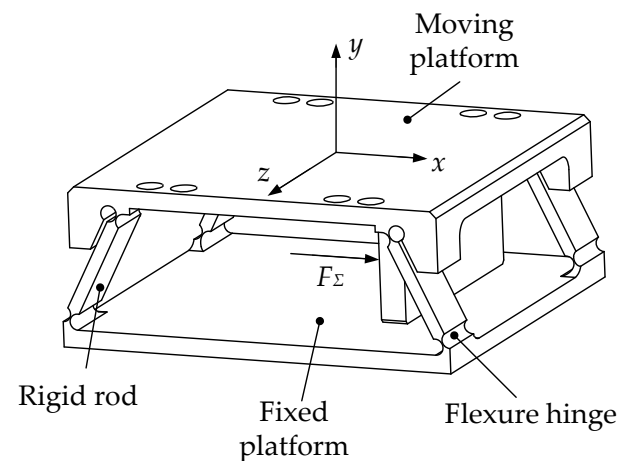


Figure 2. Optical angle nano-positioning mechanism.

The optical angle nano-positioning mechanism incorporates two sets of symmetrically arranged flexible hinges, which effectively constrain translational movements along the z -axis and rotational movements around the x -axis. When the piezoelectric (PZT) actuator exerts a driving force F_{Σ} along the x -axis, the four sets of rigid rods pivot around the flexible hinges anchored to the fixed platform. This rotational motion is subsequently transmitted to the moving platform via the flexible hinges connected to it.

2.1. Physical Design

The mechanism features a uniaxial straight circular hinge, constituting a four-link flexure hinge mechanism as shown in Figure 3, and is simplified using the pseudo-rigid body model. The four links, denoted l_i ($i = 1-4$), are interconnected via four flexible hinges. Here, l_1 is equal to l_3 , and l_4 acts as the fixed installation surface. The lines of l_1 and l_3

converge at the waist, forming an isosceles triangle with O as its vertex, where φ_0 represents the initial angle of the lower bar l_3 with respect to l_4 . The swing arm is rigidly connected to l_2 , maintaining a constant perpendicular angle to l_2 . An external force is applied to the swing arm at a distance L from the point O . When the PZT actuator drives the moving platform to displace by Δ , the rotation angles of l_1 and l_3 are denoted as φ_1 , and the rotation angle of l_2 is φ_2 , which is the mechanism output angle.

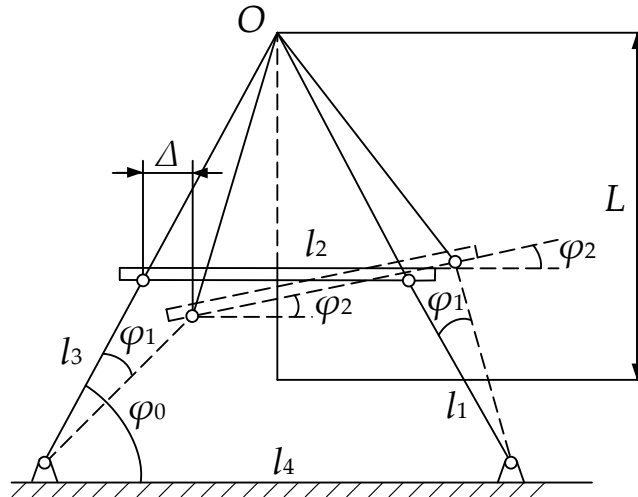


Figure 3. Schematic of the motion mechanism under the pseudo-rigid body assumption.

Following a rotation of l_3 by an angle φ_1 , it can be maneuvered based on its geometric relationship with φ_2 , which is as follows:

$$\varphi_2 = \pi - \varphi_1 - \arccos\left(\frac{l_2^2 + l_4^2 - 2l_1l_4 \cos(\varphi_0 + \varphi_1)}{2l_2\sqrt{l_1^2 + l_4^2 - 2l_1l_4 \cos(\varphi_0 + \varphi_1)}}\right) - \beta - \varphi_0 \quad (1)$$

Among which:

$$\beta = \arcsin\left(\frac{l_4 \sin(\varphi_0 + \varphi_1)}{l_1^2 + l_4^2 - 2l_1l_4 \cos(\varphi_0 + \varphi_1)}\right) \quad (2)$$

2.2. Statics Analysis

The straight circular flexure hinge, characterized by high precision, stable adjustment, and wear resistance, is illustrated in Figure 4. Within this figure, r represents the circle radius of the flexure hinge, h stands for the height of the flexure hinge, t denotes the thickness between the hinges, and b indicates the width of the flexible hinge.

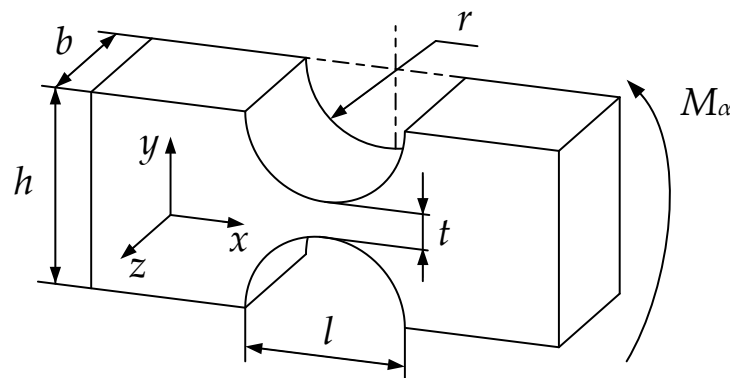


Figure 4. Optical angle nano-positioning mechanism.

The adjustment mechanism consists of eight straight circular flexible hinges, each identical in design and function. A force analysis is performed on one of these flexible hinges. Assuming the left end of the flexible hinge is fixed, the relationship between the angle α_z around the z-axis and the external torque M_α is established as follows:

$$M_\alpha = k_\alpha \alpha_z = \frac{Ebr^2}{12c} \alpha_z \tag{3}$$

where E is the elastic modulus of the material, and:

$$\begin{cases} c = \frac{2s^3(6s^2+4s+1)}{(2s+1)(4s+1)^2} + \frac{12s^4(2s+1)}{(4s+1)^{\frac{5}{2}}} \arctan \sqrt{4s+1} \\ s = \frac{r}{l} \end{cases} \tag{4}$$

The PZT actuator's thrust output, F , is entirely transformed into the flexible hinge's elastic potential energy, V . Consequently, the total energy input of the mechanism is as follows:

$$V = \int_{\Delta} F d\Delta \tag{5}$$

where Δ is the displacement corresponding to the angular displacement φ of the flexible hinges pushed by the PZT actuator. The total potential energy U of the mechanism can be obtained using the energy method:

$$U = \Sigma \frac{1}{2} k_\alpha \varphi^2 \tag{6}$$

Furthermore, based on energy conservation, we have the following:

$$M\varphi_2 = Fl\varphi_2 = \Sigma \frac{1}{2} k_\alpha \varphi^2 \tag{7}$$

$$F = \frac{k_\alpha}{2l\varphi_2} \Sigma \varphi^2 \tag{8}$$

2.3. Kinematics Analysis

Dynamic characteristics are critical benchmarks for the optical angle nano-positioning mechanism. The inclusion of a flexible structure means that design parameters significantly affect the mechanism's inherent frequency. To enhance the mechanism's overall anti-vibration capabilities, it is crucial to optimize the design of parameters that influence dynamic stiffness. In this configuration, the flexure hinge functions as a rotating spring, while other structural elements are considered rigid bodies. The dynamic model of the optical angle nano-positioning mechanism is illustrated in Figure 5.

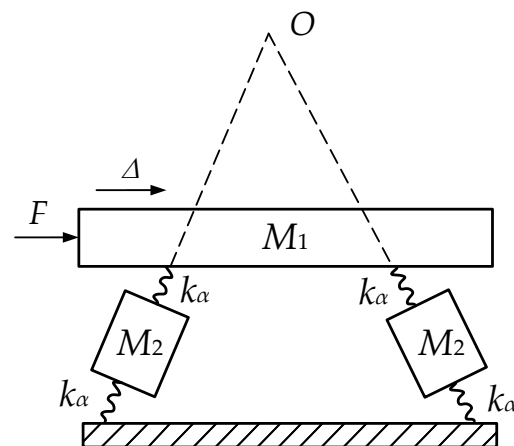


Figure 5. Dynamic model diagram of the mechanism. Flexure hinges are reduced to springs.

When the output angle is sufficiently small, the movement of the moving platform can be approximated as translational motion. Under these conditions, the kinetic energy, denoted by T , in the direction of motion is defined as follows:

$$T = \frac{1}{2}M_1^2 + 4 \times \frac{1}{2}J\phi^2 \tag{9}$$

where M_1 represents the mass of the moving platform of the optical angle nano-positioning mechanism and J signifies the moment of inertia of the rigid rod with respect to the endpoints in the direction of motion. Here, M_2 is the mass of the rigid rod and l_0 denotes the length of the rigid rod:

$$\begin{cases} J = \frac{M_2l_0^2}{3} \\ M_2 = \rho(l_1 - 2r)bt \\ l_0 = l_1 - 2r \end{cases} \tag{10}$$

Since the output angle is small enough, there is $\phi \approx \frac{\Delta}{l_1}$. By plugging in Equation 10, we can get:

$$T = \frac{M_1l_1^2}{2}\dot{\phi}^2 + \frac{2\rho(l_1 - 2r)bh^2l_1^2}{3}\phi^2 \tag{11}$$

Considering that the optical angle nano-positioning mechanism consists of eight identical hinges, the potential energy, denoted by U , in the direction of motion is defined as follows:

$$U = 8 \times \frac{1}{2}k_\alpha\phi^2 = 4k_\alpha\phi^2 \tag{12}$$

For a system with n degrees of freedom, the motion under the influence of an external force F adheres to the Lagrangian equation, which is defined as follows:

$$\frac{d}{dt}\left(\frac{\partial T}{\partial \dot{q}_j}\right) - \frac{\partial T}{\partial q_j} + \frac{\partial U}{\partial q_j} = F \quad (j = 1, 2 \dots n) \tag{13}$$

where q_j represents the generalized coordinates adopted by the system. By considering ϕ as the generalized coordinates, we can derive the following by substituting Equations (10) and (11):

$$\left(\frac{M_1}{2} + \frac{2\rho(l_1 - 2r)bh}{3}\right)l_1^2\ddot{\alpha} + 4k_\alpha\alpha = 0 \tag{14}$$

Moreover, the first-order inherent frequency, denoted as f , of the optical angle nano-positioning mechanism can be calculated as follows:

$$f = \frac{1}{2\pi} \sqrt{\frac{4k_\alpha}{\left(\frac{M_1}{2} + \frac{2\rho l_0 bh}{3}\right)(l_0 + 2r)^2}} \tag{15}$$

3. Optimization Design

3.1. Design Parameter

3.1.1. Material Parameter

The selection of materials is crucial for the performance of CMs. Excessive flexibility may reduce the overall rigidity of the mechanism, adversely affecting its dynamic performance and precision. Conversely, excessive rigidity may limit the working stroke of the mechanism. In the SRF, the mechanism is subjected to ultra-high vacuum and high-energy radiation for prolonged periods. Considering the high cost of the load crystals in the nano-adjustment mechanism, the choice of material becomes critical. Beryllium bronze (QBe2), known for its superior hardness, elastic limit, fatigue limit, wear resistance, and corrosion resistance, is an ideal material for CMs. After a solid solution treatment at 800 °C followed by an aging treatment at 330 °C, beryllium bronze demonstrates enhanced mechanical performance and corrosion resistance. The specific material performance parameters are detailed in Table 1.

Table 1. Performance parameters of beryllium bronze [30].

Density/(kg/m ³)	Elasticity Modulus/(MPa)	Poisson’s Ratio	Yield Strength/(MPa)
8300	133	0.35	750

3.1.2. Dimension Parameter

The optical angle nano-positioning mechanism is utilized within the vacuum chamber of the monochromator device at the SRF, which also accommodates other components including coarse adjustment mechanisms and cooling systems. Consequently, the dimensional requirements for the nano-adjustment mechanism are extremely stringent; an oversized nano-adjustment mechanism could interfere with adjacent devices. The specific geometric dimensions are detailed in Table 2.

Table 2. Performance parameters of beryllium bronze [31].

Length/mm	Width/mm	Height/mm	l_1 /mm	l_2 /mm	l_3 /mm	l_4 /mm
120	120	50	40	97	40	121

3.2. Design Parameter Analysis

Before undertaking multi-objective optimization, this section conducts a sensitivity analysis of the structural parameters to determine their impact on the final performance. This analysis helps identify which design parameters significantly influence performance and allows for an expanded range of choices for these parameters. The results of this sensitivity analysis, based on the previously described mathematical model, are illustrated in Figure 6. The analysis reveals that the driving force required by the mechanism is directly proportional to thickness t and width b , and inversely proportional to radius r . The parameters that significantly affect the driving force, in descending order of impact, are t , r , and b . Similarly, the parameters that most affect the inherent frequency, listed in descending order, are t , r , and b . It is evident that t has the most substantial effect on both the driving force and the inherent frequency. Therefore, the selected parameter optimization range for t should be broader: $0.2\text{ mm} < t < 0.5\text{ mm}$. For r , the optimization range should be $2\text{ mm} < r < 5\text{ mm}$. Lastly, for b , the optimization range should be $10\text{ mm} < b < 20\text{ mm}$.

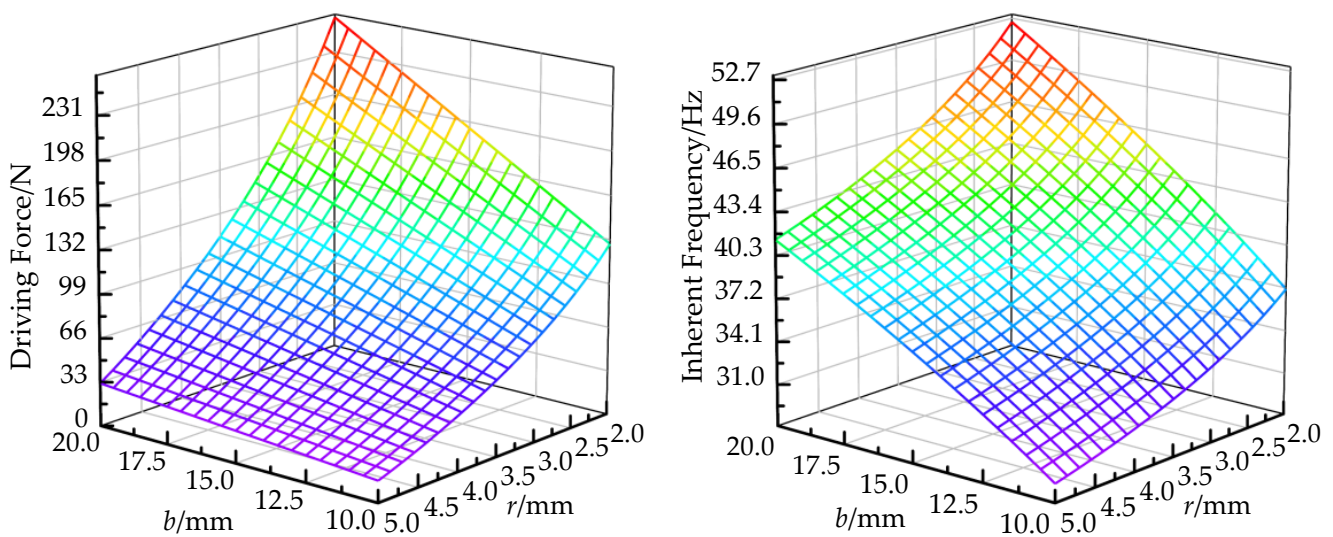


Figure 6. Cont.

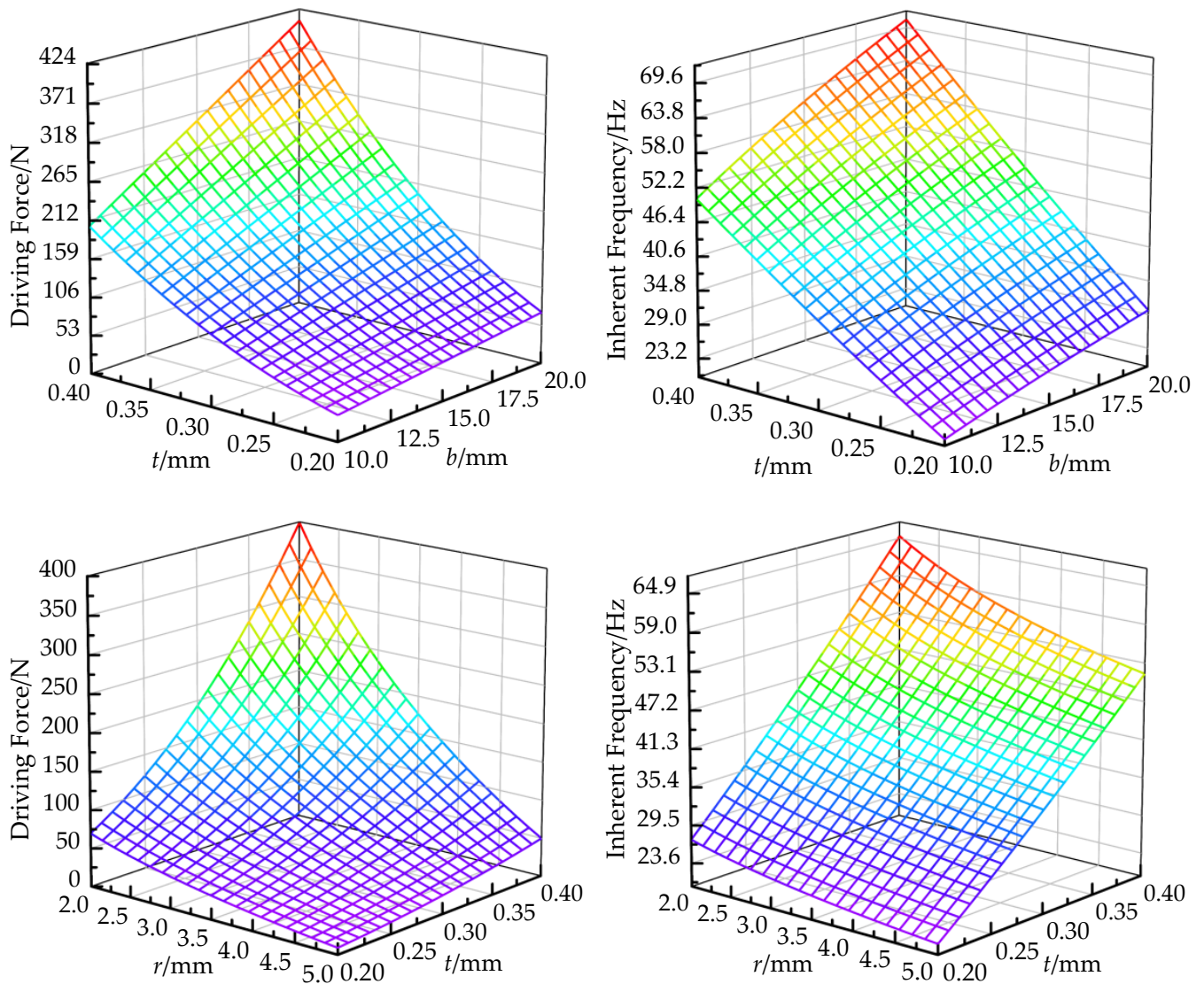


Figure 6. Sensitivity of hinge design parameters.

4. Multi-Objective Optimization Design

4.1. Objective Functions

As a mechanism that operates through material deformation, CMs should minimize the driving force required to optimize performance, necessitating low structural stiffness. However, based on the fundamental formula for inherent frequency, with a constant mass, the inherent frequency of the mechanism is directly proportional to its stiffness. A low inherent frequency may result in resonance due to external disturbances. Therefore, to ensure the mechanism’s functionality and resilience against external interference, optimization of multiple design parameters is essential. Consequently, the optimization objective for the mechanism should strive to maximize inherent frequency while minimizing the required driving force. The mathematical expression for the optimization objective is outlined as follows:

- The highest inherent frequency:

$$f_1 = \max \left(\frac{1}{2\pi} \sqrt{\frac{4k_\alpha}{\left(\frac{M_1}{2} + \frac{2\rho l_0 b h}{3}\right)(l_0 + 2r)^2}} \right) \tag{16}$$

- At the maximum output angle of the mechanism rotation, the minimum driving force is required:

$$f_2 = \min \left(\frac{k_\alpha}{2l\varphi_2} \Sigma \varphi^2 \right) \tag{17}$$

4.2. Constraints and Limitations

- Dimensional constraint.
According to the analysis in Section 3.2, the constraints on the design parameters are as follows:

$$\begin{cases} 2 \text{ mm} \leq r \leq 5 \text{ mm} \\ 10 \text{ mm} \leq b \leq 20 \text{ mm} \\ 0.2 \text{ mm} \leq t \leq 0.5 \text{ mm} \end{cases} \tag{18}$$

- Maximum stress constraint.
CMs, which rely on material deformation to achieve motion, should typically ensure that the maximum stress (σ_{\max}) endured by the material during maximum displacement remains below the yield stress (σ_y) of the material. This is crucial for guaranteeing the material’s fatigue life. In the case of this optical angle nano-adjustment mechanism, σ_{\max} is observed at the flexible hinge at the maximum output angle. The calculation formula for σ_{\max} is provided below [9,32]:

$$\left\{ \sigma_{\max} = \frac{E(1+\eta)^{\frac{9}{20}}}{\eta^2 f(\eta)} \varphi_{\max} \leq \frac{\sigma_y}{SF} = [\sigma] \right. \tag{19}$$

where $\eta = t/2r$ is a dimensionless coefficient; SF is the safety factor, and where $f(\eta)$ is as follows:

$$\left\{ f(\eta) = \frac{1}{2\eta+\eta^2} \left[\frac{3+4\eta+\eta^2}{(1+\eta)(2\eta+\eta^2)} + \frac{6(1+\eta)}{(2\eta+\eta^2)^{1.5}} \tan^{-1} \left(\frac{2+\eta}{\eta} \right)^{0.5} \right] \right. \tag{20}$$

4.3. Optimization Algorithm

As identified in the analysis of Section 3.2, the final performance indicators present potential conflicts in the selection of structural parameters. Therefore, the implementation of MOOP is essential to identify a set of feasible solutions rather than a singular optimal solution. The MOOP algorithm is executed using MATLAB on an Intel® Core™ i7-12700H CPU with 40 GB RAM. Given its prominence in extensive research literature, the NSGA-II is primarily selected. NSGA-II, an enhanced version of the original NSGA, incorporates a fast nondominated sorting method, an elite retention strategy, and a crowding distance operator. These enhancements reduce computational complexity, improve optimization efficiency, and ensure diversity within the solution population. To validate the results obtained from NSGA-II, the classic MOPSO algorithm is also employed for further verification.

5. Application of NSGA-II Algorithm for Design Problem

5.1. MOOP’s Results

In the parameter settings for NSGA-II, 300 individuals are initially randomly generated and subjected to 100 iterations (CPU time: 31.2812 s). Similarly, for MOPSO, 300 particles are initially generated and also iterated 100 times (CPU time: 42.3397 s). The Pareto frontier derived from the solutions is depicted in Figure 7. The outcomes reveal that the solutions obtained from both the NSGA-II and MOPSO algorithms are fundamentally consistent.

Table 3 lists the optimal solutions for NSGA-II and MOPSO from the perspective of each objective. This includes an evaluation of the remaining objectives for each solution, alongside the chosen set of parameters. The table also presents the solutions that offered the best balance according to their respective averages. To assess the robustness of the NSGA-II algorithm, five independent runs of the calculation were performed, with the deviation of each average displayed in Table 4.

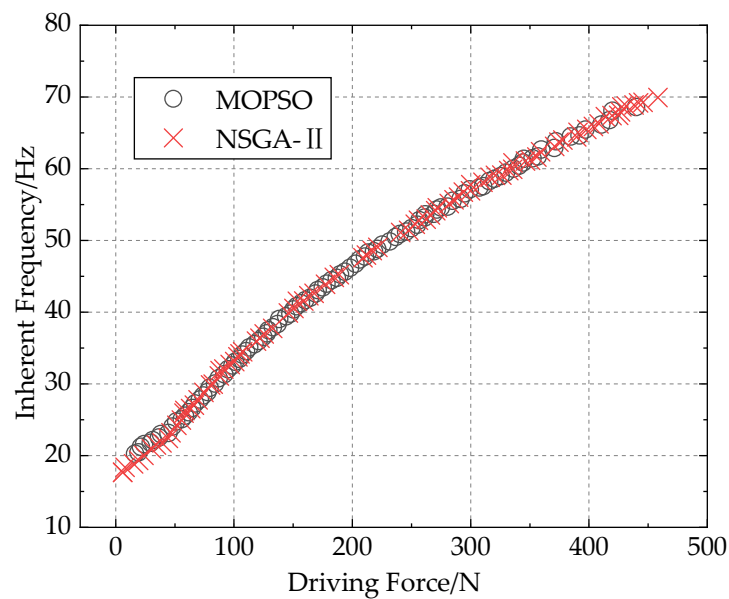


Figure 7. The problem is solved by NSGA-II and MOPSO.

Table 3. Comparison of solutions between NSGA-II and MOPSO.

Algorithm	Element	r/mm	t/mm	b/mm	Driving Force/N	Inherent Frequency/Hz	σ_{max}/MPa
NSGA-II	Best	5.00	0.38	18.71	458.23	69.92	9.56
	Worst	2.00	0.20	10.00	5.83	17.66	1.99
	Average	2.25	0.30	15.16	221.91	46.38	8.12
MOPSO	Best	4.85	0.39	19.93	451.85	71.63	9.53
	Worst	2.00	0.20	10.48	10.32	21.55	2.49
	Average	2.13	0.29	15.69	187.75	45.79	8.14

Table 4. The solution for the independent repetition of NSGA-II.

Result Number	r/mm	t/mm	b/mm	Driving Force/N	Inherent Frequency/Hz	σ_{max}/MPa
1	2.24	0.30	15.17	221.91	46.32	8.11
2	2.17	0.31	16.17	251.55	49.51	8.32
3	2.23	0.30	15.17	224.92	46.73	8.15
4	2.23	0.31	15.82	252.83	49.15	8.22
5	2.21	0.31	15.81	246.88	48.96	8.26
Expectation Value	2.22	0.31	15.63	239.62	48.15	8.22
Standard Deviation	0.0277	0.0038	0.4459	14.9963	1.4711	0.0829

For the convenience of presentation, five groups of typical representatives are selected from the Pareto solution set, as shown in Table 5.

As measured, the low-frequency vibration of the SSRF foundation is within the 1–4 Hz range, while the vibration induced by liquid nitrogen in the SSRF imaging beamline BL16U1 is at 28 Hz [33]. To ensure the reliability of the mechanism, it is noted that the first-order inherent frequency of the third solution set significantly diverges from these frequencies, and that it requires a relatively small driving force. Consequently, the second

set of representative solutions, which better aligns with these conditions, is selected as the final design scheme.

Table 5. The optimal solution rep.

	r/mm	t/mm	b/mm	Driving Force/N	Inherent Frequency/Hz	σ_{max}/MPa
1	4.79	0.20	10.11	7.93	18.38	2.56
2	3.47	0.23	12.78	82.30	29.95	7.36
3	2.88	0.29	12.86	189.07	45.21	8.31
4	2.07	0.37	14.98	310.30	58.10	9.29
5	2.00	0.39	18.71	458.23	69.92	9.56

5.2. Finite Element Calculation Verification

To further validate the accuracy of the established mathematical model, it is necessary to refine the third set of solutions listed in Table 5 using Solidworks 2021 software, tailored to meet actual engineering processing requirements. This involves reconstructing the three-dimensional model. Subsequently, simulations are conducted using ANSYS 2021R1 Workbench software. The frequency obtained is 42.599 Hz, which shows a deviation of 6.13% from the results calculated by the earlier constructed model. This discrepancy is primarily due to the omission of the hinge’s mass in simplifying the dynamic model. Figure 8 displays the finite element analysis results.

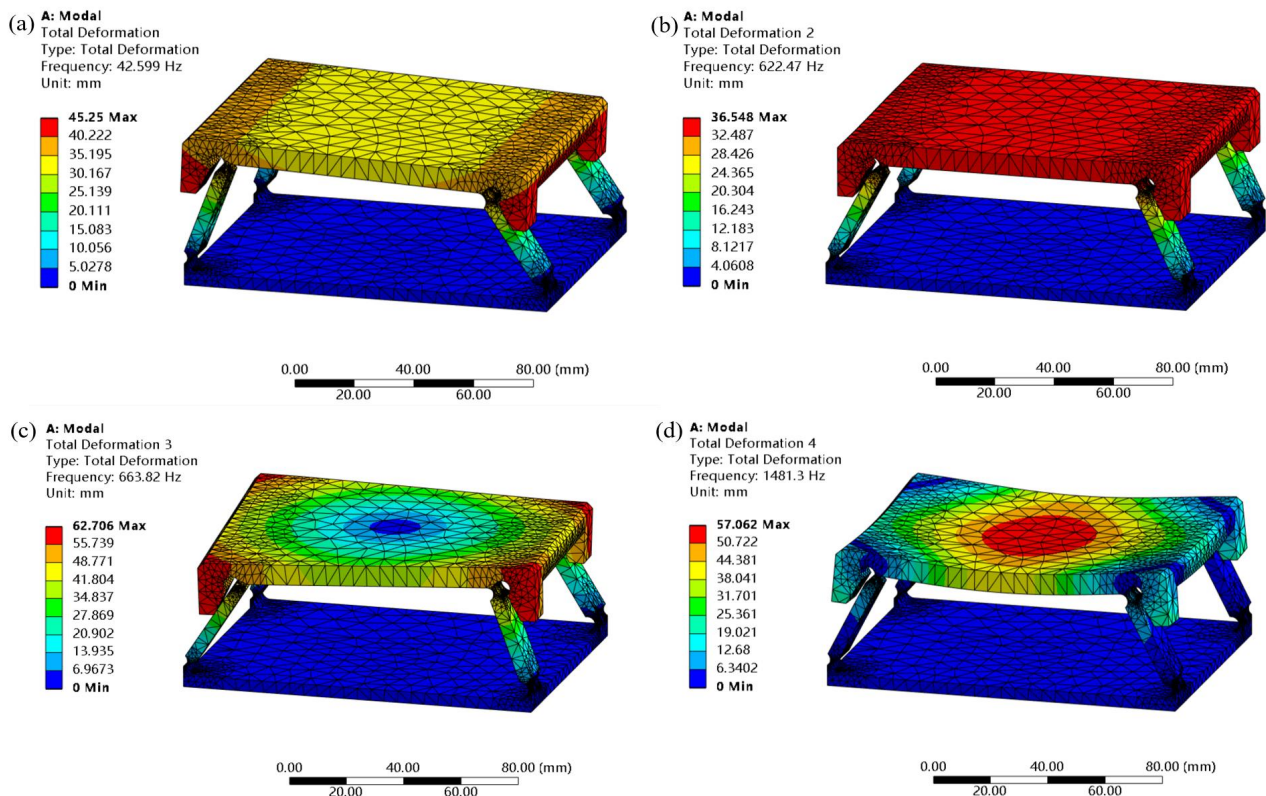


Figure 8. Modal analysis diagram. (a) First-order modal; (b) Second-order modal; (c) Third-order modal; (d) Fourth-order modal.

6. Prototype Trial Production

The data in Section 5.2 were chosen as the design parameters. QBe2 was selected for wirecut machining of the components, and the surface of the device was electroplated, as depicted in Figure 9.

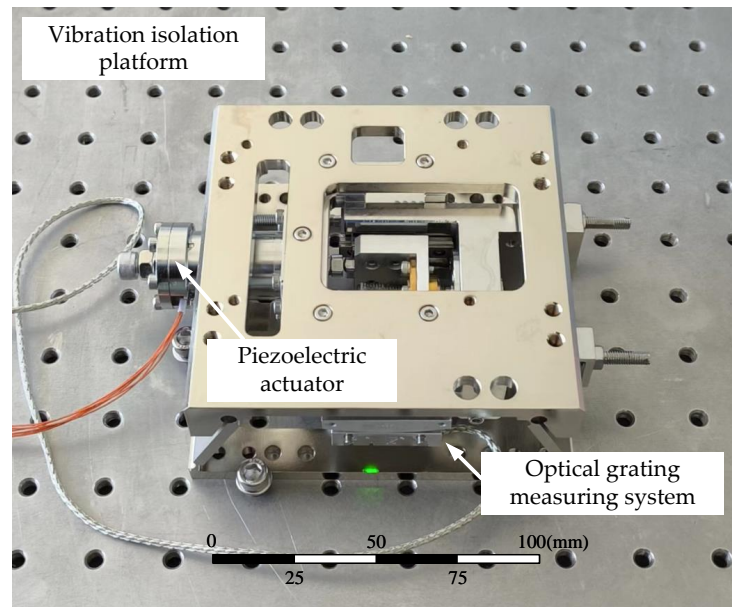


Figure 9. Prototype of the optical angle nano-positioning mechanism.

6.1. Performance Test

The minimum output resolution of the mechanism is critical for its actual working performance within the synchrotron radiation device. To assess the motion performance of the designed mechanism, an experimental setup was established. The device is secured on an optical vibration isolation platform using bolts at a room temperature of 25 degrees Celsius. This setup effectively constrains the movement of the device base in each degree of freedom and isolates potential disturbances from external sources. The piezoelectric actuator used is a high-precision model manufactured by Piezosystem Jena (model PAHL40-20SG, with a travel distance of 42 μm and a closed-loop resolution of 0.4 nm, Piezosystem Jena GmbH, Thuringia, Germany). A grating measurement system from Renishaw (model TONiC series Ti20KD, with a resolution of 1 nm, Renishaw PLC, New Mills, UK) was employed to collect the motion displacement data of the mechanism.

6.1.1. Resolution Test

In order to evaluate the prototype's minimum angular resolution, the following procedure was conducted. Firstly, the piezoelectric actuator was adjusted to a position 10 μm away from its initial position, which is closest to the actual working state. Manual control was then applied with a step size of 2 nm to investigate the mechanism's minimum resolution of motion. The grating measurement system recorded data at intervals of 100 ms. The resulting data, depicted in Figure 10, reveal a distinct step-like pattern. The minimum angular resolution of the mechanism's rotation was found to be 50 nrad, comparable to the floor noise level of the grating measurement system, which is also approximately 50 nrad.

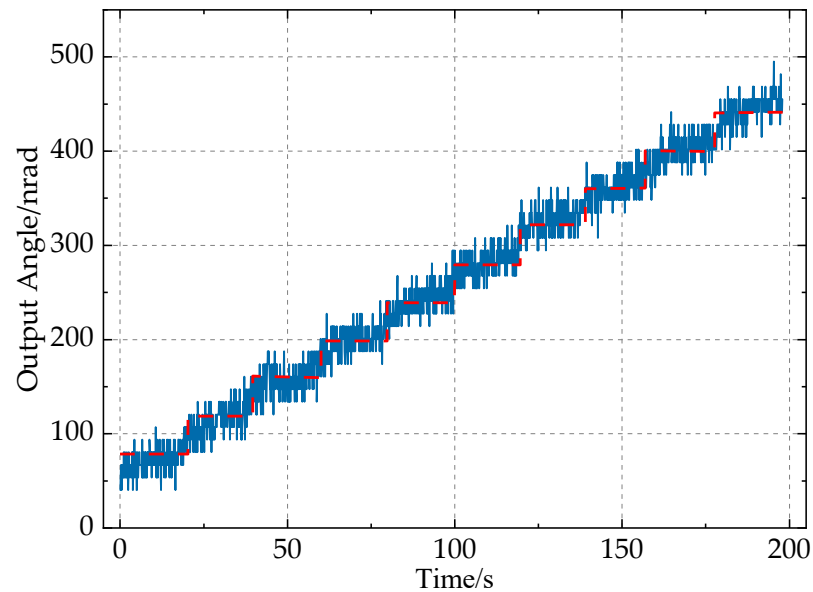


Figure 10. Resolution results.

6.1.2. Repetitive Positioning Accuracy Test

To evaluate the repetitive positioning accuracy of the mechanism, the piezoelectric actuator was cycled through positions of 0 μm , 10 μm , and 20 μm , conducting three trials at each position. The results are presented in Figure 11, where the repetitive accuracy, measured as the standard deviation, was determined to be ± 57.49 nrad at the 10 μm position.

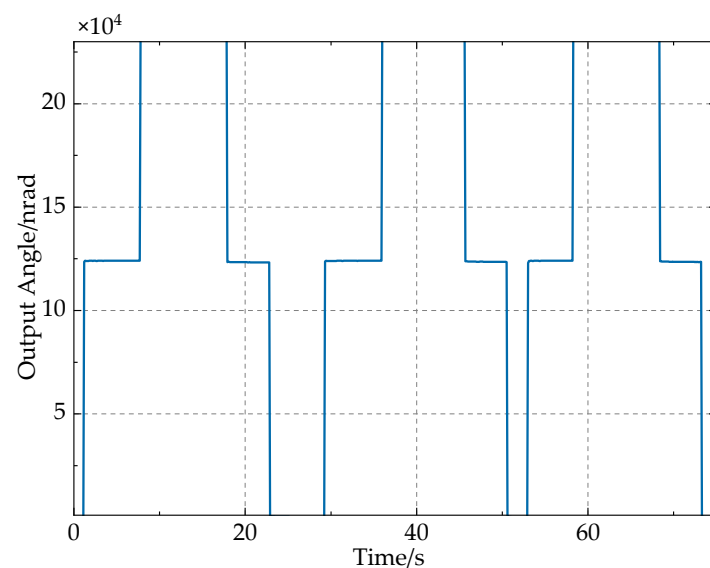


Figure 11. Repetitive positioning accuracy results.

6.2. Motor Performance Test

To verify the effectiveness of the design method proposed in this paper, an inherent frequency test of the mechanism was conducted, as depicted in Figure 12. The inherent frequency was determined using the hammer test method. For the experiment, conducted at room temperature (25 $^{\circ}\text{C}$), a 32-channel acquisition system from M+P International and data processing and analysis software from Smart Office Analyzer were utilized. Four measuring points were strategically placed on the moving platform of the mechanism. An acceleration sensor with a range of 50 g (gravity acceleration) served as the measuring point sensor to collect the vibration response signals. Each of the three axes of the acceleration sensor was

tapped three times, and the average of the three data sets was analyzed. A power spectral density (PSD) analysis of the collected data, shown in Figure 13, reveals that the PSD of the mechanism significantly peaks at 43.75 Hz, indicating the first-order inherent frequency of the mechanism. Table 3 presents a comparison between the prototype's test results and the theoretical analysis results. The test results show a discrepancy of 2.63% from the finite element analysis results and a 3.33% difference from the theoretical analysis results, thereby confirming the reliability of the finite element and theoretical analyses. The first-order inherent frequency of the mechanism is substantially higher than any frequency that could induce resonance in the synchrotron radiation device, demonstrating the mechanism's robust dynamic stability.

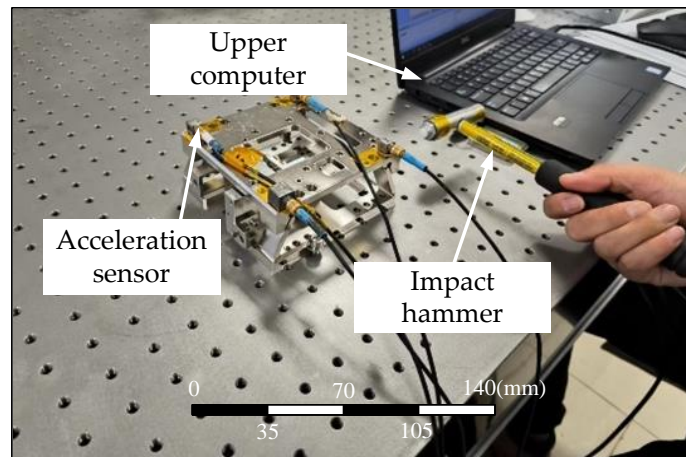


Figure 12. Inherent frequency test system.

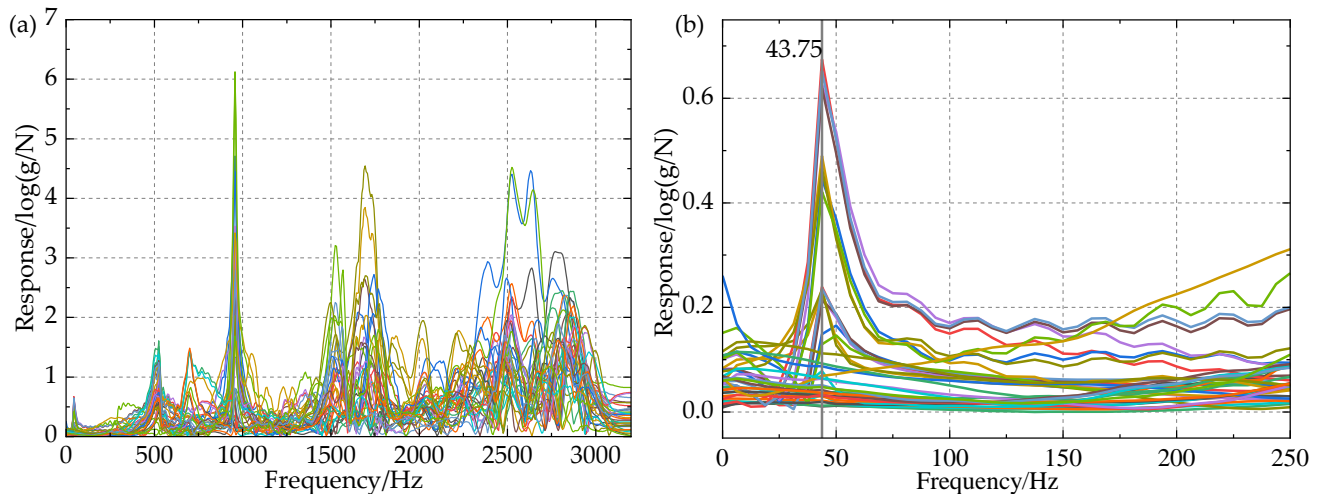


Figure 13. Spectrum diagram of the mechanism. The different colors of the lines represent data collected from different channels of the sensor. (a) All the results collected by the sensors. (b) Results before 250 Hz.

7. Conclusions

In this paper, we design an optical angle nano-positioning mechanism based on CMs to achieve ultra-high resolution nano-displacement, as necessitated by the specific engineering requirements of the SSRF. This study focuses on the design parameters of the flexible hinge, using the driving force and the inherent frequency of the mechanism as the optimization objectives to conduct multi-objective optimization. The following conclusions can be drawn from this study:

- By establishing the kinematic model based on the geometric dimensions of the mechanism, the relationship between the mechanism size and the output motion is determined.
- Analyzing the driving force required by the mechanism at the limit output angle begins with the mechanical characteristics of a single hinge. A mapping relationship between the stiffness of a single hinge and that of the entire mechanism is established.
- Utilizing the Lagrangian kinematics theory, the dynamic model of the mechanism is developed based on geometric size and mass data. The first-order inherent frequency is determined by solving the partial differential equation.
- The NSGA-II multi-objective optimization algorithm optimizes the design parameters and addresses the conflict inherent in multi-objective optimization for optical angle nano-positioning mechanisms.
- The theoretical model is validated through finite element calculations and prototype testing. The results indicate that the first-order inherent frequency of the theoretical model differs by 3.33% from the finite element analysis result and by 2.63% from the real object, substantiating the effectiveness of the proposed method.

Future studies will target more complex CMs mechanisms, aiming to achieve higher motion response, higher output resolution, and enhanced mechanism stability as objectives for further optimization.

Author Contributions: Conceptualization, H.L.; Methodology, H.L.; Investigation, Z.Z., X.L., Y.W. and Y.G.; Writing—original draft, Y.D.; Writing—review & editing, Y.D. and B.J.; Project administration, B.J. All authors have read and agreed to the published version of the manuscript.

Funding: This research was funded by Shanghai Synchrotron Radiation Facility

Institutional Review Board Statement: Not applicable.

Informed Consent Statement: Not applicable.

Data Availability Statement: The data presented in this study are available on request from the corresponding author. The data are not publicly available due to privacy.

Conflicts of Interest: The authors declare no conflict of interest.

Abbreviations

The following abbreviations are used in this manuscript:

CMs	Compliant mechanisms
SRF	Synchrotron radiation facility
APS	Argonne National Laboratory's advanced photon source
ESRF	European synchrotron radiation facility
SSRF	Shanghai synchrotron radiation facility
MOOP	Multi-objective optimization problem
PSO	Particle swarm optimization
NSGA-II	Nondominated sorting genetic algorithm-II
MOPSO	Multi-objective particle swarm optimization
PZT	Piezoelectric
QBe2	Beryllium bronze

References

1. Su, L.; Huang, G.; Huang, R.; Yang, Z. Design of a Compact Long-Stroke High-Precision Rigid-Flexible Coupling Motion Stage Driven by Linear Motore. *J. Mech. Sci. Technol.* **2022**, *36*, 5859–5870. [[CrossRef](#)]
2. Meijaard, J.P.; Van Der Wijk, V. Dynamic Balancing of Mechanisms with Flexible Links. *Mech. Mach. Theory* **2022**, *172*, 104784. [[CrossRef](#)]
3. Guo, F.; Sun, T.; Wang, P.; Liu, S.; Lian, B.; Song, Y. Multi-Stability of a Planar Three-Limb Flexible Mechanism. *Mech. Mach. Theory* **2022**, *175*, 104956. [[CrossRef](#)]
4. Cao, Y.; Wang, B.; Lin, M.; Zhang, H. Design Analysis and Optimization of Large Range Spatial Translational Compliant Micro-positioning Stage. *J. Mech. Eng.* **2020**, *56*, 71–81.

5. Chen, Y.; Lai, L.; Li, P.; Zhu, L. Full leaf-spring type spatial large-stroke parallel flexure micro-positioning stage and trajectory control. *Opt. Precis. Eng.* **2023**, *31*, 2675–2686. [[CrossRef](#)]
6. Liu, J.; Kang, S.; Chen, W.; Chen, W.; Jiang, J. A Novel Flexure-Based Register System for R2R Electronic Printing. *Microsyst. Technol.* **2015**, *21*, 2347–2358. [[CrossRef](#)]
7. ATian, Y.; Shirinzadeh, B.; Zhang, D. A Flexure-Based Five-Bar Mechanism for Micro/Nano Manipulation. *Sens. Actuators A Phys.* **2009**, *153*, 96–104.
8. Zhu, J.; Lyu, L.; Xu, Y.; Liang, H.; Zhang, X.; Ding, H.; Wu, Z. Intelligent Soft Surgical Robots for Next-Generation Minimally Invasive Surgery. *Adv. Intell. Syst.* **2021**, *3*, 2100011. [[CrossRef](#)]
9. Nguyen, V.-K.; Pham, H.-T.; Pham, H.-H.; Dang, Q.-K.; Minh, P.S. Reliability-Based Multi-Objective Optimization Design of a Compliant Feed Drive Mechanism for Micromachining. *Appl. Sci.* **2023**, *13*, 4968. [[CrossRef](#)]
10. Moschini, S.; Palpacelli, M. Insights into Bending Stiffness Modeling of Elementary Flexure Hinges. *Appl. Sci.* **2023**, *13*, 9785. [[CrossRef](#)]
11. Ren, J.; Li, Q.; Wu, H.; Cao, Q. Optimal Design for 3-PSS Flexible Parallel Micromanipulator Based on Kinematic and Dynamic Characteristics. *Micromachines* **2022**, *13*, 1457. [[CrossRef](#)]
12. Noveanu, S.; Lobontiu, N.; Lazaro, J.; Mandru, D. Substructure Compliance Matrix Model of Planar Branched Flexure-Hinge Mechanisms: Design, Testing and Characterization of a Gripper. *Mech. Mach. Theory* **2015**, *91*, 1–20. [[CrossRef](#)]
13. Schmidt, R.-H.M. Ultra-Precision Engineering in Lithographic Exposure Equipment for the Semiconductor Industry. *Phil. Trans. R. Soc. A* **2012**, *370*, 3950–3972. [[CrossRef](#)]
14. Sprouster, D.J.; Trelewicz, J.R.; Snead, L.L.; Hu, X.; Morrall, D.; Koyanagi, T.; Parish, C.M.; Tan, L.; Katoh, Y.; Wirth, B.D. Advanced Synchrotron Characterization Techniques for Fusion Materials Science. *J. Nucl. Mater.* **2021**, *543*, 152574. [[CrossRef](#)]
15. Sedigh Rahimabadi, P.; Khodaei, M.; Koswattage, K.R. Review on Applications of Synchrotron-Based X-ray Techniques in Materials Characterization. *X-ray Spectrom.* **2020**, *49*, 348–373. [[CrossRef](#)]
16. Li, J.; Huang, X.; Pianetta, P.; Liu, Y. Machine-and-Data Intelligence for Synchrotron Science. *Nat. Rev. Phys.* **2021**, *3*, 766–768. [[CrossRef](#)]
17. Aishikawa, T.; Tamasaku, K.; Yabashi, M. High-Resolution X-ray Monochromators. *Nucl. Instruments Methods Phys. Res. Sect. A Accel. Spectrometers Detect. Assoc. Equip.* **2005**, *547*, 42–49. [[CrossRef](#)]
18. Shu, D.; Anton, J.W.J.; Kearney, S.P.; Lai, B.; Liu, W.; Maser, J.; Roehrig, C.; Tischler, J.Z. Mechanical Design of Compact Vertical and Horizontal Linear Nanopositioning Flexure Stages with Centimeter-Level Travel Range for X-ray Beamline Instrumentation. In Proceedings of the 8th International Particle Accelerator Conference, Copenhagen, Denmark, 14–19 May 2017.
19. Kelly, J.; Male, A.; Rubies, N.; Mahoney, D.; Walker, J.M.; Gomez-Gonzalez, M.A.; Wilkin, G.; Parker, J.E.; Quinn, P.D. The Delta Robot—A Long Travel Nano-Positioning Stage for Scanning X-ray Microscopy. *Rev. Sci. Instruments* **2022**, *93*, 043712. [[CrossRef](#)]
20. Kearney, S.P.; Preissner, C.; Shu, D. Progress of Mechanical Design of Nanopositioning Stages at the Advanced Photon Source. *Synchrotron Radiat. News* **2018**, *31*, 38–44. [[CrossRef](#)]
21. Shu, D.; Garrett, R.; Gentle, I.; Nugent, K.; Wilkins, S. Nanopositioning Techniques Development for Synchrotron Radiation Instrumentation Applications at the Advanced Photon Source. In Proceedings of the 10th International Conference on Radiation Instrumentation, Melbourne, Australia, 27 September 2009.
22. Kearney, S.P.; Shu, D.; Toellner, T.S. The Design of a Precision Mechanical Assembly for a Hard X-ray Polarize. In Proceedings of the MEDSI2016, Barcelona, Spain, 11–16 September 2016.
23. Shu, D.; Maser, J.; Chu, Y.; Yan, H.; Nazaretski, E.; O'Hara, S.; Kearney, S.; Anton, J.; Quintana, J.; Shen, Q. Development of an Advanced Sample-Scanning Stage System Prototype for an MLL-Based Hard X-ray Nanoprobe. In Proceedings of the 10th International Conference on X-ray Microscopy, Chicago, IL, USA, 15 August 2010.
24. Shu, D.; Maser, J.; Garrett, R.; Gentle, I.; Nugent, K.; Wilkins, S. Study of Precision Weak-Link Stage Systems with Large Travel Range and Sub-Nanometer-Scale Resolution. In Proceedings of the 10th International Conference on Radiation Instrumentation, Melbourne, Australia, 27 September 2009.
25. Barrett, R.; Härtwig, J.; Morawe, C.; Rommeveaux, A.; Snigirev, A. X-ray Optics at the ESRF. *Synchrotron Radiat. News* **2010**, *23*, 36–42. [[CrossRef](#)]
26. Zeng, C.; Mao, C.; He, Y.; Li, A. Design and analysis of flexure hinge displacement mechanism with nano precision. *Nucl. Tech.* **2022**, *45*, 070101.
27. Feng, Q.; Li, Q.; Quan, W.; Pei, X. Overview of multiobjective particle swarm optimization algorithm. *Chin. J. Eng.* **2021**, *43*, 745–753.
28. Naderi, E.; Mirzaei, L.; Trimble, J.P.; Cantrell, D.A. Multi-Objective Optimal Power Flow Incorporating Flexible Alternating Current Transmission Systems: Application of a Wavelet-Oriented Evolutionary Algorithm. *Electr. Power Components Syst.* **2024**, *52*, 766–795. [[CrossRef](#)]
29. Nguyen, V.; Pham, H.; Pham, H.; Dang, Q. Optimization Design of a Compliant Linear Guide for High-Precision Feed Drive Mechanisms. *Mech. Mach. Theory* **2021**, *165*, 104442. [[CrossRef](#)]
30. Wang, R.; Zhang, X. Optimal Design of a Planar Parallel 3-DOF Nanopositioner with Multi-Objective. *Mech. Mach. Theory* **2017**, *112*, 61–83. [[CrossRef](#)]
31. Yu, J.; Bi, S.; Pei, X.; Zhao, H.; Zong, G. *Flexure Design: Analysis and Synthesis of Compliant Mechanism*, 1st ed.; Higher Education Press: Beijing, China, 2018; pp. 142–149.

32. Zhu, W.-L.; Zhu, Z.; Shi, Y.; Wang, X.; Guan, K.; Ju, B. Design, Modeling, Analysis and Testing of a Novel Piezo-Actuated XY Compliant Mechanism for Large Workspace Nano-Positioning. *Smart Mater. Struct.* **2016**, *25*, 115033. [[CrossRef](#)]
33. Fan, Y.; Qin, H.; Zhu, W.; Jia, W.; Liu, Y.; Wang, J.; Li, Z. Angular Stability Measurement of a Cryocooled Double-Crystal Monochromator at SSRF. *Nucl. Instruments Methods Phys. Res. Sect. A Accel. Spectrometers Detect. Assoc. Equip.* **2020**, *983*, 164636. [[CrossRef](#)]

Disclaimer/Publisher's Note: The statements, opinions and data contained in all publications are solely those of the individual author(s) and contributor(s) and not of MDPI and/or the editor(s). MDPI and/or the editor(s) disclaim responsibility for any injury to people or property resulting from any ideas, methods, instructions or products referred to in the content.